17th World Conference on Earthquake Engineering, 17WCEE
Sendai, Japan - September 13th to 18th 2020

SEISMIC PERFORMANCE OF A PILED RAFT FOUNDATION WITH GRID-FORM DMWS CONSIDERING SOFTENING OF STABILIZED SOIL

Y. Shigeno[(1)], K. Yamashita[(2)], J. Hamada[(3)]

[(1)] *Chief Researcher, Takenaka Corporation, shigeno.yoshimasa@takenaka.co.jp*
[(2)] *Executive Manager, Takenaka Corporation, yamashita.kiyoshi@takenaka.co.jp*
[(3)] *Chief Researcher, Takenaka Corporation, hamada.junji@takenaka.co.jp*

Abstract

Grid-form deep mixing walls (DMWs) are able to prevent liquefaction and also shear loads. Therefor the piled raft foundation with grid-form DMWs is one the most rational foundation system for a liquefiable ground. However the seismic performance of this foundation system is not well studied. In this study, seismic behavior of a piled raft foundation with grid-form DMWs under a strong earthquake is numerically evaluated. A base-isolated 12-story RC structured building supported by this type foundation in Tokyo is modeled in a 3D finite element soil structure interaction model. This model has been calibrated using the records of the 2011 off the Pacific coast of Tohoku Earthquake monitored at this building in the previous study.

The ground was modeled by a two-surface nonlinear elastic model characterized using strain dependent characteristics of soil directly as input data. As a constitutive model of the DMWs, the elasto-plastic model that is able to evaluate shear failure, tensile failure and post-peak softening was used. The post-peak softening is modeled using the distributed cracks model, and the degree of softening is assumed to be determined by the fracture energy released during the formation and opening of cracks in the DMWs. An artificial wave was used for a strong earthquake defined in the Japanese building design code for a performance design.

Based on the analysis, the tensile failure spread in the lower part of the longitudinal walls of the DMWs, which lie parallel to the shaking direction. This is due to shear deformation of the walls. And in the transverse walls, some elements at the bottom of the grid crossing corners and the middle of the grid failed. This is due to bending deformation of the walls. Tensile strength of these failed elements decreased by post-peak softening. The stress path of the elements where the tensile strength was totally lost shows that after the stress reached the tensile criterion, the criteria shrank to the 0 cohesion shear criterion. However, only a part of the elements drastically reduced their strength. This makes the grid-form DMWs keep their effectiveness of the reducing the bending moment of the piles near the pile head to an acceptable level.

Consequently, the piled-raft foundation with grid-form DWMs is found to be quite effective in reducing sectional force of piles to an acceptable level under strong earthquake, although the induced stress reaches the tensile strength and softens in some parts of them.

Keywords: piled raft foundation; deep mixing walls; post-peak softening; soil and structure interaction analysis

1. Introduction

In recent years, piled raft foundations have been used even on liquefiable sand by adding grid-form cement deep mixing walls (DMWs) [1]. Grid-form DMWs work not only as a countermeasure against liquefaction but also as a part of foundation. However the seismic behavior of this foundation is not well understood because of its complexity. The seismic behavior of this foundation has been studied by the numerical simulation of the field observation records [2, 3, 4]. And the soundness of the piles was confirmed even though the grid-form DMWs were partially failed under strong earthquakes. However, softening of the DMWs was not considered despite the fact that they are known to undergo post-peak softening. Thus in the present study, an elasto-plastic model that is able to describe post-peak softening was applied to DMWs. This paper mainly discusses on what failure and softening brings to the DMWs and to the piles during a strong earthquake.

2. Overview of building and ground

Fig. 1 shows a schematic view of the building and its foundation with the soil profile. The analyzed building is a 12-story reinforced-concrete building with a seismic base-isolation system located in Tokyo. The soil down to a depth of 44 m is very soft alluvial strata composed mainly of silty clay. The strata deeper than 44 m are diluvial sand and a gravel layer with SPT N-value of 60 or higher. The ground water table is approximately 1.8 m below the ground surface. The building is supported by a piled raft with grid-form DMWs which were employed to prevent the liquefaction of the silty sand from GL –3 m to –7 m as well as to improve the bearing capacity of the raft foundation. The spacing between the DMWs is approximately 6–9 m, and the area replacement ratio is 25%. At the time of the 2011 off the Pacific coast of Tohoku earthquake, the seismic response of the soil-foundation system and the accelerations of the ground and structure were successfully recorded [1].

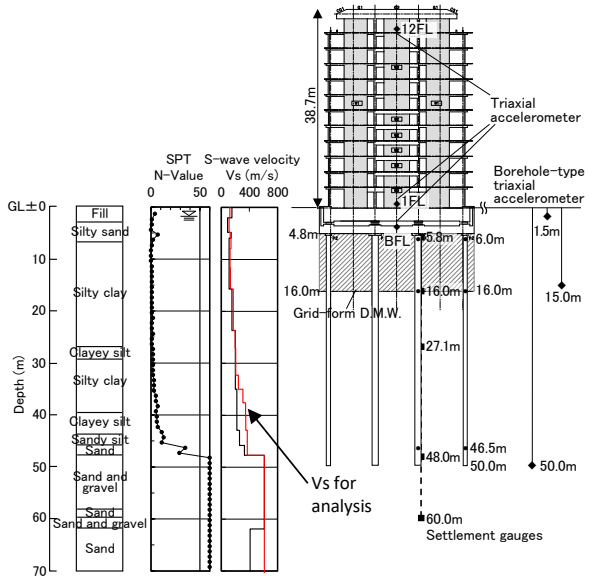

Fig. 1 – Bar macro-element

3. Analysis model

3.1 Finite element mesh

Fig 2(a) shows the finite element (FE) mesh, which has 213,622 elements and 656,543 degrees of freedom. The superstructure is modeled using elastic bars and shells, and the piles are modeled using elastic bars. The piles are all ready made and the upper 12 m of the piles are SC piles, and the lower 33 m are PHC piles, with

diameters from 0.8 to 1.2 m. The raft is modeled using elastic solid elements with the modulus of concrete. Rayleigh damping is applied to these components at a damping ratio of 2%. Fig 2(b) shows a top view of the FE mesh beneath the raft. To consider the shape and volume of the piles, cavities in the shape of the piles are made in the model. The nodes of the piles and the adjacent ground nodes at the same depth are bound by rigid bar elements. The base isolation system is modeled using a tri-linear spring. The lateral boundaries are periodic boundaries, and are positioned 60 m outside of the building. The bottom is a viscous boundary at a depth of 75 m from the ground surface. The software is an in-house program called MuDIAN [5]. It is parallelized using the hybrid parallel method and is able to analyze a large-DOF model at high speed [6].

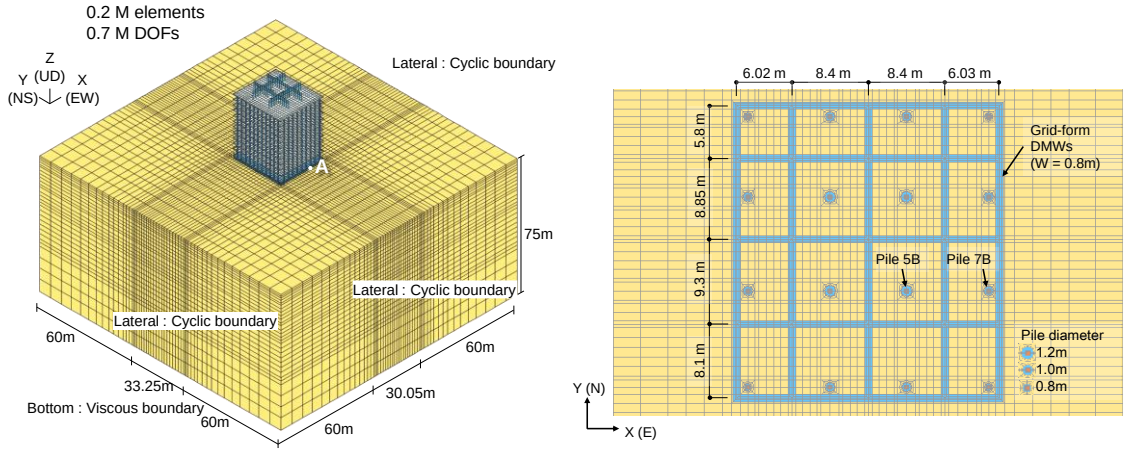

(a) General view (b) Magnified top-down view under the raft

Fig. 2 – Finite element model

3.2 Input motion

An artificial wave is used for a strong earthquake called 'Level 2 earthquake' that is officially notified in Japanese building design code for performance design. The recurrence interval is considered to be about 500 years. The wave is defined by the acceleration response spectrum as shown in Fig. 3. The input wave is generated using phase data. In this paper, the wave is generated using the Hachinohe phase data at the Tokachi-Oki Earthquake in 1968 recorded at Hachinohe bay. Hachinohe wave is the typical subduction zone earthquake, and strong motion continues during long period. The NS direction wave is used, and one directional input motion (NS direction) is applied in this study. Fig. 4 shows the input motion, and the maximum acceleration is 337 gal.

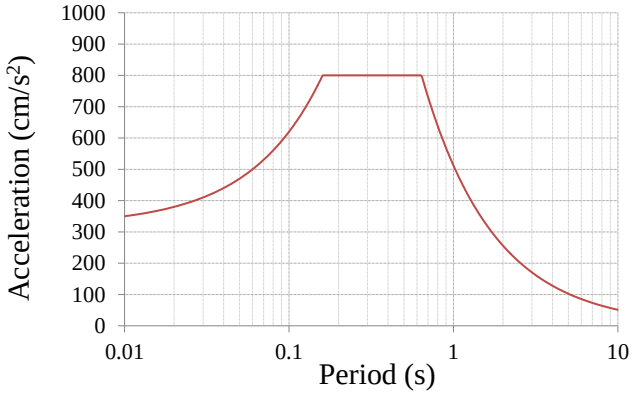

Fig. 3 – Acceleration response spectrum of Level 2 earthquake (h = 5%)

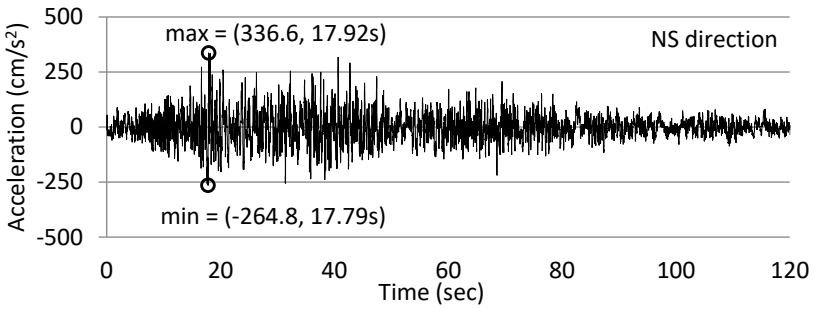

Fig.4 – Input acceleration wave (Hachinohe wave) at a depth of 75 m (2E)

3.3 Soil model

The Yoshida model for multiple-dimensions [7] was used for the soil. The Yoshida model is a two-surface nonlinear elastic model and is characterized using G–γ and h–γ characteristics directly as input data. Fig.5 shows the strain dependent characteristics of the soil at this site. The profile of the shear wave velocity for the analysis is shown in Fig. 1 as the red line. The profile was obtained by calibration analysis using the observed records [4]. Liquefaction was not considered in this study.

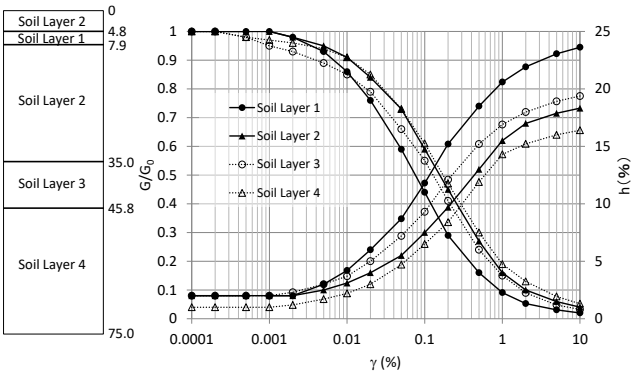

Fig. 5 – Strain dependent characteristics of soil

3.4 Constitutive model for stabilized soil

The model proposed by Namikawa et al. (2007) [8] was used for the stabilized soil. The model has three characteristics. (1) Two different failure criteria are employed for tensile and shear failure. (2) Strain-softening is considered after the peak strength. (3) The smeared crack concept is used in the strain-softening rules.

The tensile criterion considering softening using the damage parameter ω is expressed as Eq. 1 (note that tension is positive).

$$\frac{2\left(J'_2\right)^{\frac{1}{2}}}{\sqrt{3}}\sin\left(\theta+\frac{2\pi}{3}\right)+\sigma_m=T_f\left(1-\omega\right) \tag{1}$$

where J'^2 is the second invariant of deviatoric stress, θ is the Lode angle, σ_m is mean stress, T_f is the tensile strength, ω is the damage parameter.

The damage parameter ω for tensile failure is expressed as a function of the maximum plastic principal strain ε_1^p using a 1/4 bilinear model obtained by analyzing the bending test of the stabilized beam.

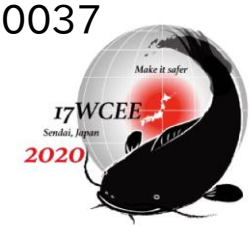

(2)

$$\omega = l_m \frac{T_f}{G_f}\left(\varepsilon_1^p - \varepsilon_{1peak}^p\right) \quad 0 \le \omega \le 0.75$$

$$\omega = \frac{12}{17} + \frac{1}{17} l_m \frac{T_f}{G_f}\left(\varepsilon_1^p - \varepsilon_{1peak}^p\right) \quad 0.75 < \omega \le 1.0$$

where, G_f is the fracture energy, $\varepsilon_1{}^p{}_{peak}$ is the peak plastic principal strain and l_m is a parameter that depends on the mesh size of the finite element model. The parameter l_m is introduced to remove the mesh size dependency of the strain localization.

The shear criterion is based on the Mohr–Coulomb criterion. The yielding function considering strain-hardening and softening is expressed as Eq. 3.

$$\left(J'_2\right)^{\frac{1}{2}} + \left(\frac{\sqrt{3}\sin\phi}{\sqrt{3}\cos\theta - \sin\theta\sin\phi}\right)\left\{\sigma_m - \frac{c(1-\omega)}{\tan\phi}\right\}k_y = 0 \tag{3}$$

where c is the cohesion, ϕ is the friction angle, k_y is an internal state variable describe the hardening. The variable k_y determines the loading surface size, and it is assumed to be the hyperbolic function of the second invariant of the deviatoric plastic strain $\bar{\varepsilon}^p$ as Eq. 4.

$$\frac{k_y - k_0}{k_f - k_0} = \frac{\dfrac{\bar{\varepsilon}^p}{e_y}}{1 + \dfrac{\bar{\varepsilon}^p}{e_y}} \qquad k_0 = \frac{T_f}{\sigma_m - \dfrac{\alpha c}{\tan\phi}} \tag{4}$$

where k_f is the coefficient of the normal-yield surface, e_y and α are hardening parameters.

From the experimental results, the damage parameter ω for shear was assumed as Eq. 5.

$$\omega = 1 - \exp\left\{-\frac{R_l\left(\bar{\varepsilon}^p - \bar{\varepsilon}^p{}_{peak}\right)}{e_r}\right\} \qquad R_l = \frac{l_m}{l_c} \tag{5}$$

where l_c is the characteristic length that specifies the size of the failure region, and e_r is the material parameter. The damage parameter ω is common to both the tensile and shear criterion, and the loading surface reduces in both criteria after the stress reaches the strength. Fig. 6 shows the two failure criteria of the model and how they reduce by softening.

The Building Center of Japan (BCJ) (2002) [9] has proposed that the design standard compressive strength F_c of the stabilized soil is to be set 1.3 standard deviations below the average compressive strength of in-situ core samples. From 36 core samples aged 28 days, F_c was set to 2.6 MPa [10]. The other parameters were also adopted the BCJ proposal as shown in Table 1. The initial shear modulus G_0 was determined from the calibration analysis of the observation records of the 2011 off the Pacific coast of Tohoku earthquake [4]. As for the initial stress in the DMWs, an isotropic stress of 170 kPa was applied based on the measured vertical pressure 300 kPa between the raft and the DMWs [1] and the horizontal stress calculated using the coefficient of earth pressure at rest. Stiffness proportional damping of 5% was applied to the DMWs considering the previous study [3] and no strain-hardening assumption for the tensile criterion. Softening highly depends on G_f, l_m and l_c. G_f was referred to Namikawa (2006) that was from the concrete beam bending test. The value of l_m was determined from the typical mesh size of DMWs. The value of l_c was determined assuming the total distributed crack width within the typical mesh of DMWs. However, further investigation is needed to determine l_m and l_c. Other model parameters were also referred to Namikawa (2006) [11] as given in Table 2.

Fig. 7 shows the simulation result of the uniaxial extension test. Where σ_1 is the maximum principal stress, and ε_1 is the maximum principal strain. The properties given in Table 1 and 2 were used. The initial stress was zero, and the extension was applied under strain-constrained condition. The stress degraded after it reached the initial tensile strength σ_{t0} = 520 kPa.

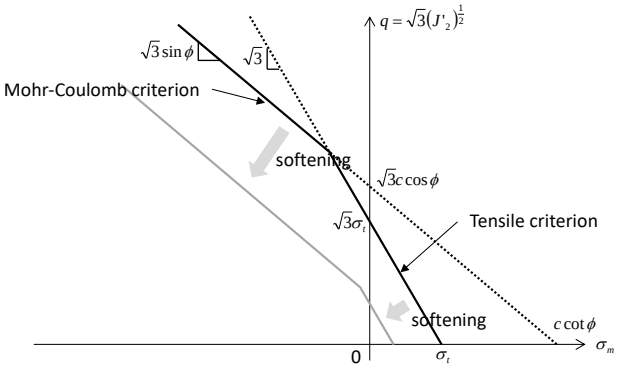

Fig. 6 – Criteria of Namikawa model (tension is positive)

Table 1 – Strength parameters of the stabilized soil

Compressive strength	F_c	MPa	2.60
Tensile strength	$0.2F_c$	kPa	520
Cohesion	$0.3F_c$	kPa	780
Friction angle	ϕ	degree	30
Poisson's ration	ν		0.26
Density	ρ	t/m^3	2.00
Initial shear modulus	G_0	MPa	500

Table 2 – Parameters of the Namikawa model

Hardening parameter	α		0.9
Hardening parameter	e_y		0.0001
Fracture energy	G_f	N/m	20.0
Softening parameter for shear	e_r		0.4
Dilatancy coefficient	D_c		0.0
Characteristics length of mesh	l_m	m	1.0
Localization size	l_c	mm	50

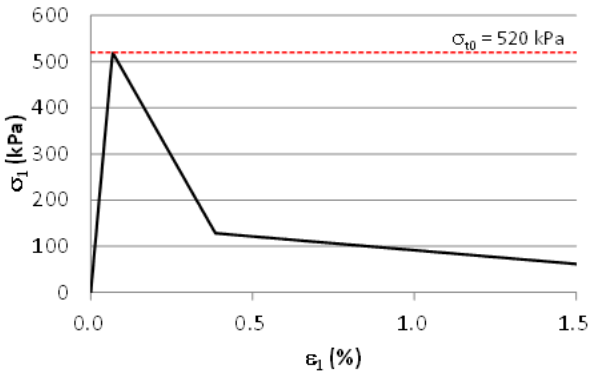

Fig. 7 – Results of numerical uniaxial extension test of stabilized soil

4. Results

Fig. 8(a) shows the profiles of the peak acceleration at the center of the superstructure and the raft together with the ground at point A (Figure 2(a)). The results are shown by the red lines. The black lines are the results of the case without DMWs that was analyzed to clarify their effect of the DMWs. The peak acceleration profile of the soil column model ("Free Field") is also plotted by the blue line. The PGA at the surface of the soil column was 296 Gal. In the case with DMWs, the peaks were 272 Gal at the raft and 130 Gal on the first floor. Fig. 8(b) shows the profiles of the peak displacement relative to GL –49.9 m. The peak displacements of the raft were –10.8 and 8.0 cm with DMWs, and –15.7 and 10.1 cm without DMWs. Thus, the ground deformation beneath the raft was clearly reduced by the DMWs, and this affects the sectional force of the piles.

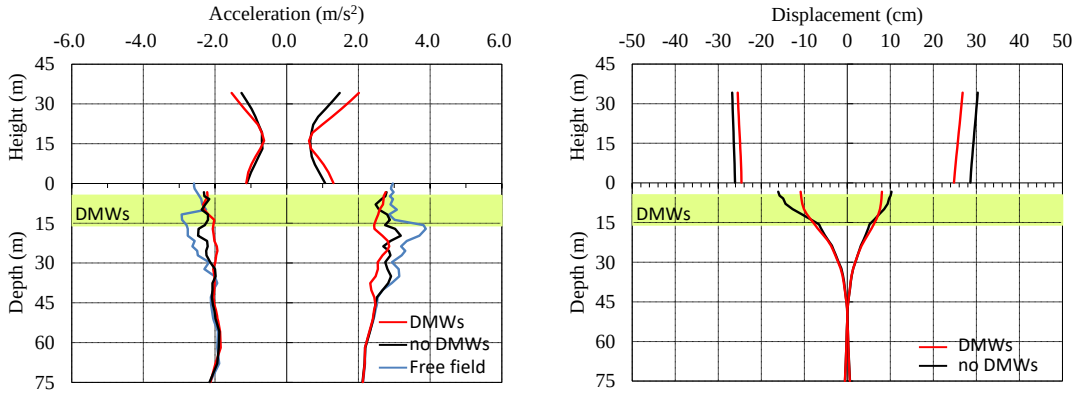

(a) Acceleration (b) Displacement relative to GL –49.9 m

Fig. 8 – Peak response profiles of the center of the superstructure and the ground at point A

First, the stress state of the DMWs is described. Fig. 9 shows the extent of the tensile failure in the grid-form DMWs during the earthquake in two different angled view from above. The elements are colored according to the number of Gauss points where the induced stress reached the tensile strength. The number of Gauss points in each element is eight, and then the maximum value is 8. In the longitudinal walls which lie parallel to the shaking direction, tensile failure occurred mostly in the lower part. This is due to shear deformation. In the upper part of the longitudinal walls, few tensile failure elements were observed because the deformation was restricted by the raft. In the transverse walls, the elements at the bottom of the grid crossing corners and the bottom of some centers of the walls failed. This is due to bending of the transverse walls. Fig. 11 shows how the each directional walls deformed at 18.6 s that was the peak y deformation time of the DMWs.

Fig. 10 shows the residual tensile strength of the each element at the final time step. The elements whose tensile strength decreased due to softening are colored. Deep blue means the tensile strength is almost lost. Softening begins after stress reaches the tensile strength. Therefor colored zone is similar to Fig. 9 although graduations of color are different. As shown in the figure, tensile strength is almost lost at the lower corners of the outer longitudinal walls. This is due to the stress concentration during the deformation. The stress concentration occurs because the rigidity of the ground under the toe of the DMWs is higher than the ground above. The high deformability is another reason. Because the softening progresses as plastic stretch strain increases as specified in Eq. 2. However, most of the elements maintained high tensile strength, despite the stress reached the tensile strength in quiet a lot elements as shown in Fig. 9.

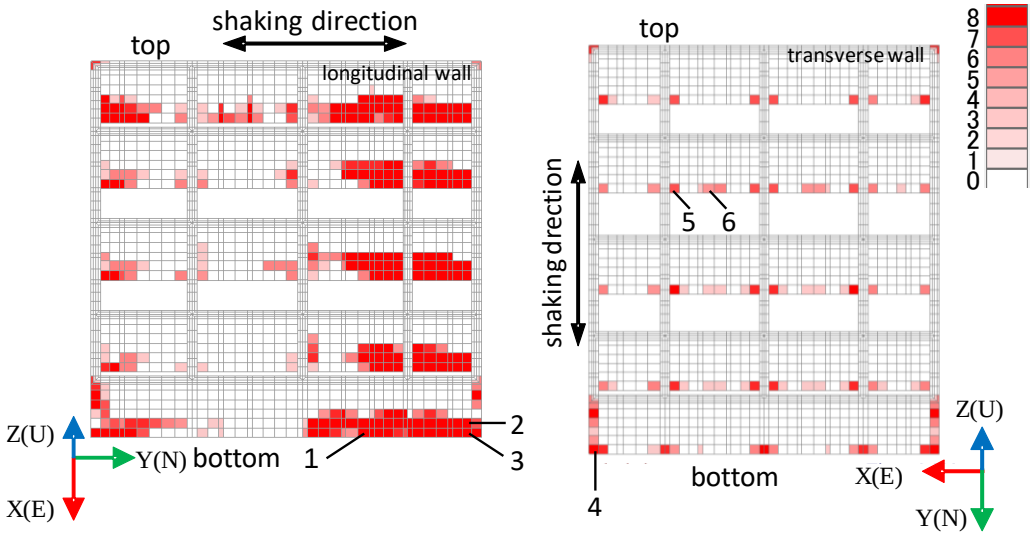

Fig. 9 – Color map of the number of tensile failure Gauss points in grid-form DMWs (two angled views from above)

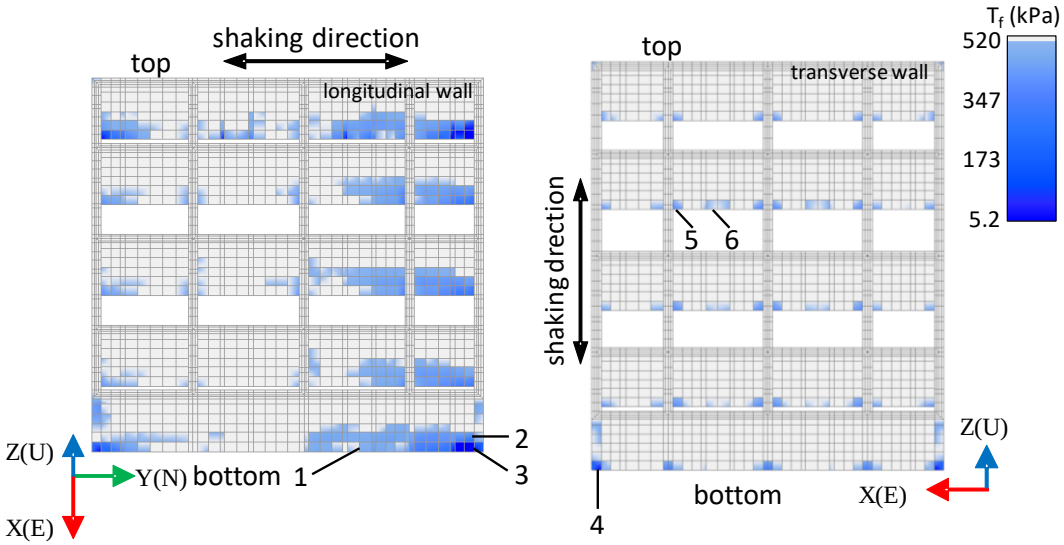

Fig. 10 – Color map of residual tensile strength at the final step (two angled views from above)

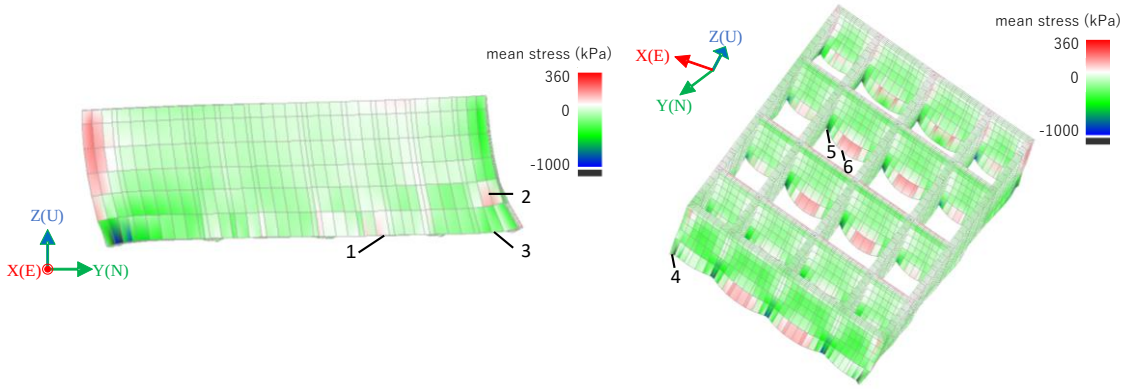

Fig. 11 – Deformation of DMWs and color map of mean stress at time 18.6 s

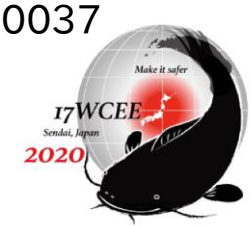

Fig 12 shows the stress path and the time history of the tensile strength of labeled elements in Fig. 9 and 10. The Gauss point where the tensile strength decreased most in each element was chosen. Fig. 12(a) is the stress path in the case which the DMWs are linear to clarify the intense of stress. Fig. 12(b) is the nonlinear case. These paths are from time 0 to 40 s because significant softening occurred during this period. Red line in the stress path is the tensile criterion when the stress first reached the tensile strength. The red dot line in the time history is the initial tensile strength.

In element 1, the stress path of the linear case became 'V' shape. The path repeated the shearing in the tensile side (point 2) and the shearing in the compression side (point 4) centering the initial point 0. In the nonlinear case, the stress reached the tensile criterion at point 1, and the path moved toward point 2 according to the associated flow rule. The softening occurred during these points. The decreasing rate to the initial strength was as small as 0.08. The path moved to point 3 by unloading, and moved to point 4 by the shearing in the compression side. The stress was within the criteria after point 2, and the path became 'V' shape. The center of the path moved from pint 0 to point 3 due to the dilatancy between point 1 and 2.

The path of element 2 is somewhat complicated. The stress first reached the tensile strength at point 1. The path move toward point 2 same as element 1. Large softening occurred during point 1 and 2, and the criteria shrank. The stress reached the shrunk tensile criterion again at point 3, and small softening occurred. The stress reached the tensile criterion again at point 4, and the path moved toward point 5. The stress moved to on the shrunk shear criterion between point 5 and 6. The blue lines are the shrunk criteria at point 6. Point 6 was on the cross point of the shrunk tensile and shear criteria. Large softening occurred again during point 4 and 6. The ratio of the residual tensile strength to the initial strength was 0.44.

In element 3 and 4, the stress paths differed from the other elements due to large softening. In these elements, the equivalent stress on the tensile side was very large in the linear case. The stress first reached the tensile criterion at point 1 and the path moved toward point 2 same as element 1 and 2. At point 2, the stress moved on the shrunk shear criterion due to the large softening and dilatancy. Loading went on until point 3. The tensile strength decreased to 0.32 of the initial value at this point. Unloading continued until point 4. The stress path moved to point 5 by the shearing on the compression side. Although non-associated flow rule was adapted on the shear failure, the mean stress moved much toward the compression side due to the elastic increment of the compressive stress during point 4 to 5. The tensile strength degraded to 0.01 of the initial value at point 5. This ratio is the lower limit given as the input data. The shear criterion became Mohr-Coulomb criterion with the 0 cohesion at this point as shown in the blue line. After point 5, the stress path became 'V' shape with the blue line as the upper limit. In the elements where the tensile strength is almost lost, the criterion becomes the shear criterion with the initial friction angle and 0 cohesion.

In element 5 and 6, tensile failure occurred due to the bending deformation of the transverse wall. Element 5 was at the root of bending. The equivalent stress on the tensile side was large next to element 3 and 4 as shown in the linear case. And the equivalent stress on the compression side was the largest among these elements. Therefor the stress reached the tensile criterion at point 1 and also reached the shear criterion at point 4. The shrunk criteria of point 4 are plotted in blue lines. The tensile criterion is larger at point 4 than that of at point 1 due to the Lode angle. The tensile softening occurred from point 1 to point 2, and the small tensile softening occurred at point 5 where tensile failure occurred again. The shear softening at point 4 was slight. The tensile strength decreased to 0.71 of the initial value. Element 6 was at the top of bending deformation. The equivalent stress on tensile side was small as shown in the linear case. And the stress path in the nonlinear case was similar as element 1. The residual tensile strength was 0.98 of the initial value.

These results shows that the degree of the softening depends on the magnitude of the equivalent stress on the tensile side when it is seen in the liner case. And significant softening was localized at the lower corner of the outer longitudinal walls. Therefor the intensely colored regions in tensile failure points map (Fig. 9) do not represent the parts where the strength is completely degraded. This only means the stress reached the red line in the stress path figure at all Gauss point. It is important to note that the elements which lost all the tensile strength were localized, and many elements kept relatively high residual strength even though all Gauss points tensile failed.

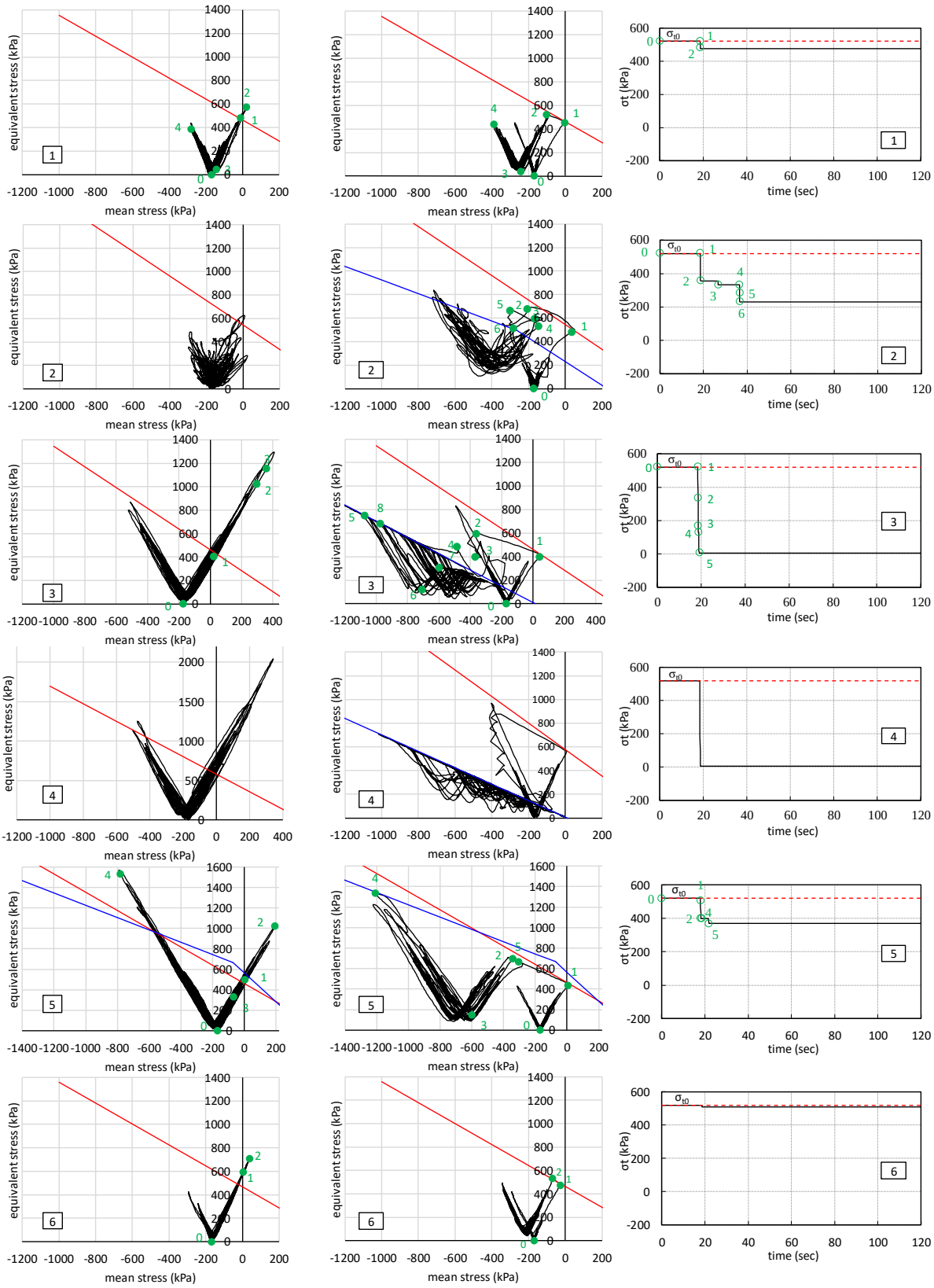

(a) Linear case (b) Non-linear case (c) Time history of tensile strength

Fig. 12 – Stress path and tensile strength of the DMWs elements specified in Fig. 9 and 10

Next, the section force of piles is described. Fig. 13 shows the profiles of the peak bending moment in piles 5B and 7B (see Fig. 2(b)). The section force of piles is also compared to the case without DMWs in the black lines. The moment near the pile head in the case with DMWs was remarkably smaller than that in the case without DMWs. In the case with DMWs, the deformation of the soil enclosed by the DMWs was small and resulted in a small bending moment near the pile head. However, the moment at the bottom of the DMWs was large, because the high rigidity of the DMWs at this point produced a large curvature displacement. In contrast, in the case without DMWs, the deformation of the soil near the pile head was large and asymmetric in the peak profile. This results in a large and asymmetric bending moment at the pile head. These results show the same tendency as the case without softening of the DMWs [3].

Fig. 14 shows the relationship between the axial force and the bending moment of piles 5B and 7B, with the design interaction curves of the steel pipe–concrete composite (SC) piles [12] that were used upper 12 m. The axial force is the sum of the statically measured pile head load and the dynamic increment in the analysis, and the bending moment is the maximum value along the SC pile. The results show that the maximum bending moments with DMWs were below the allowable criterion. In contrast, the maximum bending moments without DMWs were close to the ultimate criterion. This shows that the DMWs are quite effective at reducing pile bending moment to an acceptable level, although the induced stress in the DMWs partially reached the tensile strength and softened under a strong earthquake load.

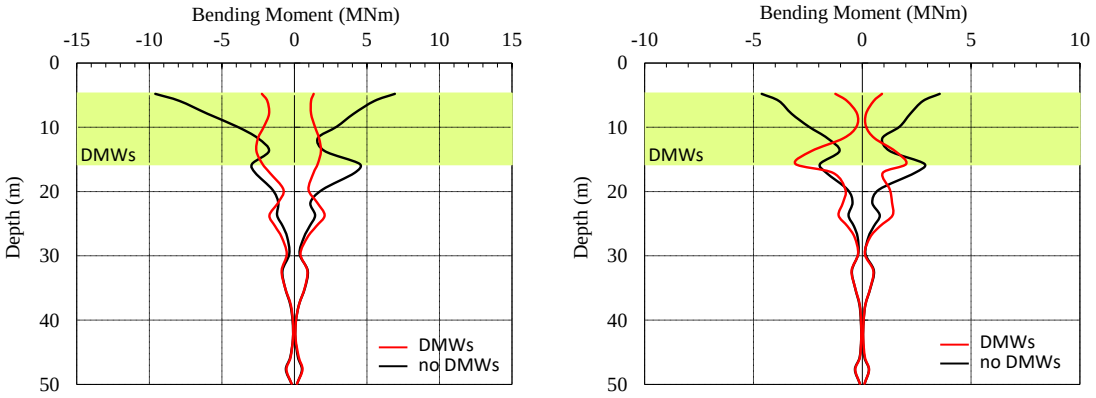

(a) Pile 5B (b) Pile7B

Fig. 13 – Profiles of peak bending moment of piles

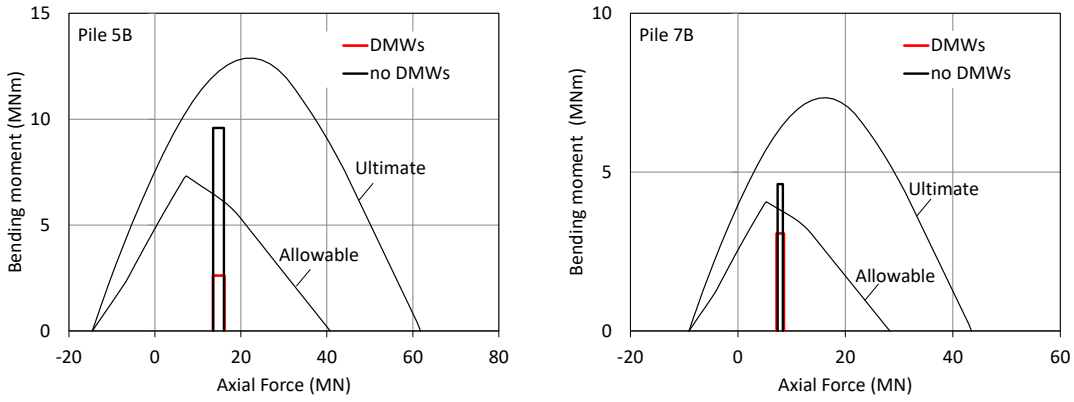

(a) Pile 5B (b) Pile7B

Fig. 14 – Calculated maximum moment along the pile and the design N–M interaction curves of SC piles

5. Conclusion

The seismic response analysis of a piled raft foundation with grid-form DMWs was carried out using a three-dimensional nonlinear finite element model under a strong earthquake load considering the post-peak softening of the DMWs. As a result, the induced stress reached the tensile strength and softening occurred in some lower parts of the DMWs. However, the bulk of the DMWs maintained a high tensile strength, and the DMWs were still able to reduce the bending moment of the piles to an acceptable level. This indicates that grid-form DMWs can be designed more rationally by applying a performance-based design method in which a partial failure of the DMWs is accepted. To verify the numerical analysis results, further study based on physical modelling such as using a geotechnical centrifuge would be required.

6. References

[1] Yamashita, K., Hamada, J. & Tanikawa, T. (2016). Static and seismic performance of a friction piled combined with grid-form deep mixing walls in soft ground. *Soils & Foundations* 56(3), 559-573.

[2] Yamashita, K., Hamada, J., Onimaru, S. & Higashino, M. (2012). Seismic behavior of piled raft with ground improvement supporting a base-isolated building on soft ground in Tokyo. *Soils & Foundations* 52(5), 1000–1015.

[3] Yamashita, K., Shigeno, Y. Hamada, J. & Chang, D. W. (2018). Seismic response analysis of piled raft with grid-form deep mixing walls under strong earthquakes with performance-based design concerns. *Soils & Foundations.* 58(1), 65-84.

[4] Shigeno, Y., Yamashita, K., Hamada, J. & Nakamura, N. (2017). Numerical evaluation of seismic performance of piled raft with grid-form DMWs under large earthquake loads. *Design and analysis of pile raft foundations -2017*, 109-127, Taipei: Tamkang University Press.

[5] Shiomi, T., Shigeno, Y. & Zienkiewicz, O. C. (1993). Numerical prediction for model No. 1. *Verification of Numerical Procedures for the Analysis of Soil Liquefaction Problems* (ed. by Arulanandan & Scott), 213-219, Balkema.

[6] Shigeno, Y., Hamada, J. and Nakamura, N. (2014). Hybrid parallelization of earthquake response analysis using K computer, *Proc. of the 14th IACMAG*. Kyoto, Japan

[7] Tsujino, S., Yoshida, N. & Yasuda, S. (1994). A simplified practical stress-strain model in multi-dimensional analysis. *Proc. of International Symposium on Pre-failure Deformation Characteristics of Geomaterials*, Sapporo, Japan, 463-468.

[8] Namikawa, T. & Mihira, S. (2007). Elasto-plastic model for cement-treated sand. *Int. J. Numer. Anal. Mech. Geomech*. 31, 71-107.

[9] Building Center of Japan. (2002). Specification for design and quality control of cement treated soil (in Japanese).

[10] Yamashita, K., Tanikawa, T., Shigeno, Y. and Hamada, J. (2015). Vertical load sharing of piled raft with grid-form deep mixing walls, *Conference on Deep Mixing 2015*, San Francisco, USA, 437-446.

[11] Namikawa, T. & Koseki, J. (2006). Experimental determination of softening relations for cement-treated sand. *Soils & Foundations* 46(4), 491-504.

[12] Japan Pile Corporation. (2011). *Pile foundation design materials* (in Japanese).

